Generation and Calibration of High-Resolution DEM From Single-Baseline Spaceborne Interferometry: The "Split-Swath" Approach

Daniele Mapelli, Andrea Monti Guarnieri, *Member, IEEE*, and Davide Giudici

I. Introduction

THE generation of digital elevation models (DEMs) through single-pass synthetic aperture radar (SAR) interferometry is a well-known application that has been demonstrated by the success of the Shuttle Radar Topography Mission (SRTM) [1], [2] mission and the recent results from TANDEM-X [3]. While these DEMs meet the requirements of a wide community of users, they pave the way for better DEM with finer planimetric and altimetric resolutions, attaining the best resolution achievable by optical DEM in highly contrasted scenes.

The generation of such DEMs is made possible by the 500-MHz bandwidth nowadays available for civil applications and may be even better in the future. However, the finer resolution results in smaller swaths and then in more stringent requirements for the calibration of the interferometer's parameters [4].

In this paper, we make specific reference to a single-pass spaceborne SAR interferometer exploiting two antennas with a boom, like SRTM [1], [2] or the Ka-band concepts proposed in literature [5]–[7]. In such systems, one of the major challenges in the generation of DEM with metric accuracy is the estimation of baselines, which is subject to mechanical vibrations with hertz or subhertz frequencies [8] and where the limited extent of the boom demands for accuracies within tens of micrometers. The paper focus is the frequent estimation of the baselines required by the boom dynamic. The calibration of baselines is made by means of ground control point (GCP) that we assume to take from a coarse, prior DEM, like STRM.

A mathematical model is developed to assess the final DEM quality by accounting for interferometric coherence and, jointly, the accuracy in baseline calibration that, in turn, depends on the following: 1) the quality of the GCPs; 2) its location with respect to the target of interest; and 2) the geometry of the acquisition system. A closed-form solution, achieved under the simplified assumption of regular gridded GCPs at near-zero height, identifies the swath width as a major limitation. In conventional stripmap mode, the swath gets narrow as the resolution improves [9], then hindering the precise baseline estimation. To avoid the problem, the "split-swath" technique is then proposed as an alternative to stripmap, where the two interferometric images are simultaneously acquired by scanning, for example, in ScanSAR [10], [11] or TOPSAR [12] mode, two swaths separated by several tens of kilometers across track; see Fig. 1.

The method exploits the same idea of Wavemill altimeter–interferometer [13], to calibrate the across-track baseline by angular difference, yet with a very different configuration (shown in Fig. 1). It is found that, through the exploitation of the distance between the two split swaths, this calibration technique can reach micrometric accuracy in a time shorter than boom dynamics.

This paper is organized as follows. Sections II and III recall the model for the 3-D location by single-pass interferometry and estimate accuracy by linearizing around the working point. This linearization is then used in Sections IV and V to derive the performance model respectively in a closed-form approximation and in the exact numerical expression for both stripmap and split-swath cases. Finally, as study case, the performances of a Ka-band interferometer are provided in Section VI and

Manuscript received January 31, 2012; revised September 26, 2012, April 24, 2013, and August 6, 2013; accepted September 6, 2013. This work was supported in part by the European Space Agency project: "Study into Ka-band SAR."

D. Mapelli and D. Giudici are with Aresys (a Politecnico di Milano spin-off company), 20134 Milan, Italy (e-mail: daniele.mapelli@aresys.it; davide.giudici@aresys.it).

A. Monti Guarnieri is with the Dipartimento di Elettronica e Informazione, Politecnico di Milano, 20133 Milan, Italy, and also with Aresys (a Politecnico di Milano spin-off company), 20134 Milan, Italy (e-mail: monti@elet.polimi.it).

Color versions of one or more of the figures in this paper are available online.

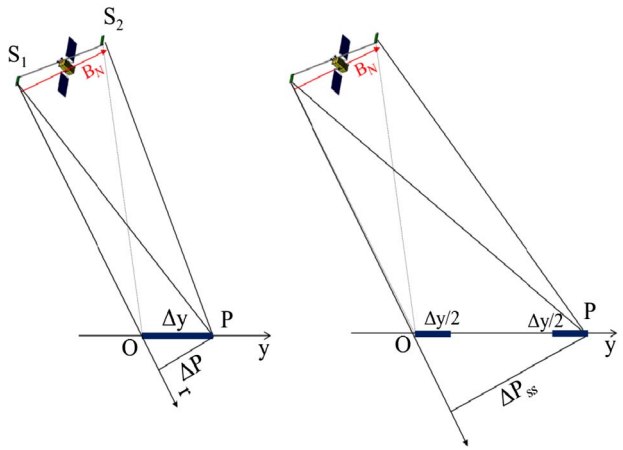

Fig. 1. Sketch of the interferometric geometry in the case of the (left) single-swath and (right) split-swath configurations.

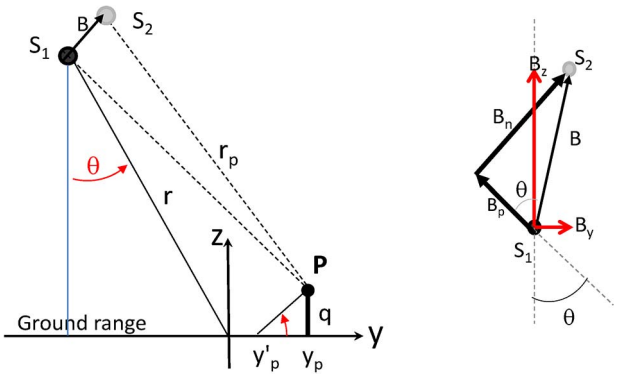

Fig. 2. Sketch of the interferometric geometry and baseline components, in the y, z plane orthogonal to the track (i.e., zero-Doppler plane).

compared with the results achieved by a numerical simulation of a complete chain including interferogram generation and DEM estimation.

II. Localization by Interferometry

Let us consider the interferometric system whose geometry is represented in Fig. 2. The two-antenna phase centers S_1 and S_2 (see [14] and [15] for general introductions on SAR interferometry) and the target of interest P are located in the plane orthogonal to the track—we assume zero-Doppler pointing. The reference system is assumed local to the target and close enough to ignore variations of the incidence angle. We assume that x, y, and z are the three DEM coordinates to be retrieved along track, ground range, and height, respectively.

In SAR interferometry, the image acquired by the first sensor (i.e., S_1) is referred as the "master image" (or simply "master"), while the data from the second sensor S_2 are said "slave image" (or simply "slave"). SAR interferometry is performed by coregistering the two images in range and azimuth and then taking the difference of the phases between the master and the slave images. We may well approximate the phase by the scalar product between the slant range versor and the baseline [15]

$$\Delta\phi = -\frac{2p\pi}{\lambda}\Delta R = -\frac{2p\pi}{\lambda}\underline{R}^{\mathrm{T}}\cdot\underline{B}. \tag{1}$$

with λ being the wavelength, $p = 1$ for the bistatic, and $p = 2$ for the monostatic configurations. We use single underline for vectors, double underline for matrices, and $^{\mathrm{T}}$ for transposition. The range versor and the baseline vectors involved in (1) can be expressed for the generic target on the DEM, $P(x_p, y_p, z_p)$ in Fig. 2, as follows:

$$\begin{aligned}\underline{\mathrm{R}} &= \frac{\underline{\mathrm{P}}-\underline{\mathrm{S}}_1}{|\underline{\mathrm{P}}-\underline{\mathrm{S}}_1|} = \frac{1}{r_p}[y_p + r\sin\theta \quad z_p - r\cos\theta]^{\mathrm{T}}\\ \underline{\mathrm{B}} &= [B_y \quad B_z]^{\mathrm{T}}\\ &= [B_n\cos\theta - B_p\sin\theta \quad B_n\sin\theta + B_p\cos\theta]^{\mathrm{T}}.\end{aligned} \tag{2}$$

B_n and B_p are the normal and parallel components of the baseline. The difference of distances ΔR in (1) derives from the geometry in Fig. 2

$$\begin{aligned}\Delta R(P) &= \underline{R}^{\mathrm{T}}\cdot\underline{B}\\ &= \frac{B_y\left(y'_p + \frac{z}{\tan\theta} + r\sin\theta\right) + B_z(z - r\cos\theta)}{\sqrt{\left(y'_p + \frac{z}{\tan\theta} + r\sin\theta\right)^2 + (z - r\cos\theta)^2}}\\ &= \frac{z_p B_z}{r_p} + \frac{y_p B_y}{r_p} - \frac{r}{r_p}(-B_y\sin\theta + B_z\cos\theta)\\ &= \frac{B_n}{r_p}z_p\sin\theta + \frac{B_n}{r_p}y_p\cos\theta - \frac{B_p}{r_p}y_p\sin\theta\\ &\quad + \frac{B_p}{r_p}z_p\sin\theta - \frac{r}{r_p}B_p\\ &\approx \frac{B_n}{r_p}\frac{z_p}{\sin\theta} + \frac{B_n}{r_p}y'_p\cos\theta - \frac{B_p}{r_p}y'_p\sin\theta - B_p\end{aligned} \tag{3}$$

where we have introduced the following change of variable:

$$y'_p = y_p - \frac{z_p}{\tan\theta} \tag{4}$$

to correct range by the shift introduced by height z_p (see Fig. 2). The first term in (3) accounts for the contribution due to target height, the second and third account for a rotation due to the flat terrain, and the last is a constant shift due to the parallel baseline. The differential delay (3) is proportional to the interferogram's phase measured for the Pth target and can then be combined with the other two observables, i.e., the azimuth and the slant range, leading to the equations ruling target location

$$\begin{aligned} x_p &= x_{zd}\\ r + y'_p\sin\theta &= r_P\\ \frac{B_n}{r}\frac{z_p}{\sin\theta} + y'_p\frac{B_n}{r}\cos\theta - y'_p\frac{B_p}{r}\sin\theta - B_p &\approx k\phi \Leftrightarrow k = \frac{\lambda}{2p\pi}.\end{aligned} \tag{5}$$

The equations system (5) relates the unknown three target coordinates (x_p, y'_p, z_p) to the three observables on the right side: the zero-Doppler along-track position x_{zd}, the range distance r_P, and the interferometric phase ϕ. These observables are affected by noise.

We remind that the approximations involved in (5) (particularly the constant incidence angle) are sufficient for the evaluation of accuracies in the target coordinates $P(x_p, y'_p, z_p)$ but not for their precise determination, for which an exact closed-form solution is given in [16]. We will remove this approximation in Section V.

III. Model for Local Accuracy

The accuracy in locating each target is dependent not only on the noises affecting the observables but also on the accuracy of the knowledge of the system parameters involved in (5). The most sensitive ones are indeed the baselines, as a slight change in the phase center would significantly impact the interferometric phase in (5).

In order to cope with this, the approach here proposed uses a prior coarse-resolution DEM as a grid of GCPs, to be exploited for precise baseline calibration.

We derive the overall accuracy of the DEM by properly accounting for both the noise in the observables, namely, the interferogram phase, range, and azimuth, and the GCPs, used for calibration, that are themselves affected by statistical uncertainty. To get that, we linearize the localization system (5) near the solution: the exact target location, $\underline{P} = \underline{P}_0$ and to the exact baselines $\underline{B} = \underline{B}_0$, as we are interested in metric or submetric errors

$$\begin{aligned} \underline{\Delta}_d &= \left.\frac{\partial f}{\partial \underline{P}}\right|_{\underline{P}=\underline{P}_0,\underline{B}=\underline{B}_0} \underline{\Delta}_p + \left.\frac{\partial f}{\partial \underline{B}}\right|_{\underline{P}=\underline{P}_0,\underline{B}=\underline{B}_0} \\ \underline{\Delta}_B &= \underline{\underline{J}}_P \underline{\Delta}_P + \underline{\underline{J}}_B \underline{\Delta}_B \end{aligned} \tag{6}$$

where $\underline{\underline{J}}_P$ is the (3×3) Jacobean obtained by differentiating the three equations in each of the three target coordinates and, similarly, $\underline{\underline{J}}_B$ is the (3×3) Jacobean obtained by differentiating in the three baseline components (including the along-track—here assumed null). The (3×1) vectors $\underline{\Delta}_d$, $\underline{\Delta}_p$, and $\underline{\Delta}_B$ represent the errors in the SAR observables due to noise, the target location error that we are interested in, and the error in the baselines, respectively.

The bias in location error is derived by taking the mean in (6)

$$E[\underline{\Delta}_P] = \underline{\underline{J}}_P^{-1} E[\underline{\Delta}_d] - \underline{\underline{J}}_P^{-1} \underline{\underline{J}}_B E[\underline{\Delta}_B]. \tag{7}$$

The target location, and then the DEM to be computed, is estimated without bias if $E[\underline{\Delta}_p] = 0$. A sufficient condition from (7) is for that both errors on the observables $\underline{\Delta}_d$ (range, Doppler, and interferometric phase) and on the baselines $\underline{\Delta}_B$ have zero mean. At a first approximation, we can assume that SAR data are mainly affected by thermal noise, so that $E[\underline{\Delta}_d] = 0$. Then, if we calibrate baselines by an unbiased prior DEM, like SRTM [1], [17], then the computed DEM will be unbiased.

However, small biases, on the order of centimeters, are caused by tropospheric and ionospheric propagation, earth tides, and local phenomena like volume penetration (frequency dependent), as discussed in [18]–[21]. Aside from those compensations proposed in literature, the prior unbiased DEM could be further exploited through (7) to mitigate residual biasing affecting the final DEM.

A. Variance

The evaluation of the variances of horizontal and vertical locations (5) is carried out in the general case in the Appendix, where the covariance of the estimates $\underline{\underline{C}}_{\Delta_P} = E[\underline{\Delta}_P \underline{\Delta}_P^{\mathrm{T}}]$ is expressed as a function of the covariance of the observables, the covariance of the GCP, and their locations with respect to the target of interest. The results there achieved can be used to take account of not only the baselines but also the uncertainties in other parameters, like orbits and precise timing.

Here following, we will evaluate the variance of the vertical location, sensitive to the baselines, by assuming at first perfect knowledge of the baselines and then relaxing this assumption.

1) Height Accuracy With Known Baselines: If all parameters are known, the rightmost term in (6) is null. The vertical accuracy, the one that we are interested here, is derived from (4a) in the Appendix

$$\begin{aligned} \sigma_z^2 &= \left(\frac{B_y}{B_n}\right)^2 \sigma_r^2 + \left(\frac{\sin\theta}{B_n} r \left(\frac{\lambda}{2p\pi}\right) \sigma_\phi\right)^2 \approx \frac{q_{2\pi}}{2\pi}\sigma_\phi \\ \sigma_\phi^2 &= \frac{1-\gamma^2}{2\gamma^2 \cdot ML} \\ q_{2\pi} &= \frac{\lambda}{p}\frac{r\sin\theta}{B_n} \end{aligned} \tag{8}$$

where $q_{2\pi}$ is the height of ambiguity and σ_ϕ^2 is the Cramer–Rao bound for the interferometric phase dispersion [15]. The approximated expression in (8) is the leading one in interferometry [14], [15]. The contribution of the standard deviation of the range location σ_r is negligible in most cases. In fact, it is a fraction of the slant range resolution in the SAR image, but it is further reduced when looks are averaged in the interferogram generation. Nonetheless, it may be relevant in altimetric–interferometric missions, where centimetric accuracies are needed [19]. In those cases, even if hundreds of looks are averaged, there remains a residual contribution due to the atmospheric phase screen whose standard deviation is 3–5 cm, considering just the wet component of the troposphere [20], [21].

2) Local Accuracy With Calibration: Here, again, we limit our analysis to height but assume that baselines are unknown. The variance of the DEM height is derived by differentiating the target height, (3), with respect to both the phase and the baselines. We get the generalization of (8), which is given by (9), shown at the bottom of the page.

The origin of the y-axis is placed at the beginning of the swath. The first contribution in (9) is the leading one, the DEM random error due to the interferometric phase noise, whereas the last two are those discussed in [22]: a DEM stretch due to errors in the normal baseline and an error dependent on the range and incidence angle (through $q_{2\pi}$), which introduces a

$$\sigma_z^2 = \left(\frac{q_{2\pi}}{2\pi}\sigma_\phi\right)^2 + \underbrace{\left[\left(\frac{z_p}{q_{2\pi}} + \frac{2}{\lambda} y_p' \frac{B_n}{r}\cos\theta\right)\frac{q_{2\pi}}{B_n}\sigma_{B_n}\right]^2 + \left[\left(\frac{2q_{2\pi}}{\lambda} + \frac{2}{\lambda} q_{2\pi}\frac{y_p'}{r}\sin\theta\right)\sigma_{B_p}\right]^2}_{\sigma^2_{Z,\mathrm{geometry}}} \tag{9}$$

DEM rotation. To get a rough idea of the accuracy needed in the *normal baseline*, we impose that the second component in (9) is negligible with respect to the first

$$\left(\frac{z_p}{q_{2\pi}}+\frac{2}{\lambda}y'_p\frac{B_n}{r}\cos\theta\right)\frac{q_{2\pi}}{B_n}\sigma_{B_n}\ll\frac{q_{2\pi}}{2\pi}\sigma_\phi=\sigma_z$$
$$\Rightarrow\frac{\sigma_{B_n}}{B_n}\ll\frac{\sigma_z}{z_p+y'_p\frac{\sin 2\theta}{2}}. \quad (10)$$

The normal baseline accuracy becomes critical when the baseline is itself small, like for a system with a boom in Ka-band, or even more in an airborne system [19].

IV. Baseline Calibration From Reference DEM: Single Swath

Let us approach the estimation of baselines from the *a priori* DEM (or a set of GCPs) and analyze the accuracy achievable, i.e., $\sigma_{B_n}\sigma_{B_p}$ to be used in (9). The interferometric phase in correspondence to the GCP is affected by an error in both horizontal and vertical locations. We apply the change of coordinate (4) to (2) and then differentiate by assuming small errors in both baselines ΔB_n and ΔB_p and GCP locations Δy and Δz. If we approximate for $y, z \ll r_p$ and $r\approx r_p$, we get

$$k\Delta\phi\approx\frac{\partial\Delta R}{\partial z_p}\Delta z+\frac{\partial\Delta R}{\partial y_p}\Delta y+\frac{\partial\Delta R}{\partial B_n}\Delta B_n+\frac{\partial\Delta R}{\partial B_p}\Delta B_p$$
$$k\Delta\phi\approx k\frac{2\pi}{q_{2\pi}}\Delta z+\frac{B_n\cos\theta}{r_p}\Delta y$$
$$+\left(\frac{z_p}{r_p\sin\theta}+\frac{y'_p}{r_p}\cos\theta\right)\Delta B_n-\Delta B_p \quad (11)$$

where $k=\lambda/2p\pi$. We get a system with as many equations as GCP Ng

$$\begin{bmatrix}\frac{y'_{g1}\cos\theta_{g1}}{r_{g1}}+\frac{z_{g1}}{r_{g1}\sin\theta_{g1}} & -1\\ \cdots & \cdots\\ \frac{y'_{gNg}\cos\theta_{Ng}}{r_{gNg}}+\frac{z_{gNg}}{r_{gNg}\sin\theta_{gNg}} & -1\end{bmatrix}\begin{bmatrix}\Delta B_n\\ \Delta B_p\end{bmatrix}=k\begin{bmatrix}\Delta\phi\\ \cdots\\ \Delta\phi\end{bmatrix}$$
$$-\frac{2\pi k}{q_{2\pi}}\begin{bmatrix}\Delta z\\ \cdots\\ \Delta z\end{bmatrix}+\frac{B_n\cos\theta}{r_p}\begin{bmatrix}\Delta y\\ \cdots\\ \Delta y\end{bmatrix} \quad (12)$$

having assumed the same quality Δy, Δz for all GCPs. The system can be written in matrix formulation

$$\underline{\underline{J}}_B\underline{\Delta B}=k\underline{\Delta\phi}-k\frac{2\pi}{q_{2\pi}}\underline{\Delta z}+\frac{B_n\cos\theta}{r_p}\underline{\Delta y}. \quad (13)$$

This can be pseudoinverted for the baseline error, as discussed in (6a) in the Appendix

$$\underline{\Delta B}=\underline{\underline{J}}_B^{\perp}\left(k\underline{\Delta\phi}-k\frac{2\pi}{q_{2\pi}}\underline{\Delta z}+\frac{B_n\cos\theta}{r_p}\underline{\Delta y}\right) \quad (14)$$

and then exploited to evaluate the covariance

$$E[\underline{\Delta B}\underline{\Delta B}^{\mathrm{T}}]=\sigma_T^2\underline{\underline{J}}_B^{\perp}\underline{\underline{J}}_B^{\perp}=\sigma_T^2\left(\underline{\underline{J}}_B\underline{\underline{J}}_B^{\mathrm{T}}\right)^{-1} \quad (15)$$

where

$$\sigma_T^2=k^2\sigma_\phi^2+k^2\left(\frac{2\pi}{q_{2\pi}}\right)^2\sigma_z^2+\left(\frac{B_n\cos\theta}{r_p}\right)^2\sigma_y^2. \quad (16)$$

For a rough evaluation, we can provide a closed-form solution by assuming that the reference DEM is at height $z=0$ and that the N_g samples in range are equally spaced by d and close enough to assume equal distance (being the swath in high-resolution SAR small). Then, we approximate each equation in (12)

$$\underline{\underline{J}}_B\underline{B}=\begin{bmatrix}n\frac{d}{r}\cos\theta & -1\end{bmatrix}\begin{bmatrix}B_n\\ B_p\end{bmatrix}$$
$$=k\Delta\phi-\frac{2\pi k}{q_{2\pi}}\Delta z+\frac{B_n\cos\theta}{r_p}\Delta y. \quad (17)$$

The baseline variance is derived from (15) as follows:

$$\sigma_{Bn}^2\approx\frac{12}{N_g^3-N_g}\frac{r^2}{d^2\cos^2\theta}\sigma_T^2$$
$$\sigma_{Bp}^2\approx\frac{4}{N_g}\sigma_T^2 \quad (18)$$

where σ_T^2 is to be evaluated by replacing in (16) σ_y^2 and σ_z^2 with the horizontal and vertical variances of the prior DEM. We remind that the expression is approximated for small swaths (constant incidence angle). The baseline accuracy follows the classical expression for a linear regression that scales with N_g^{-3}, inverse to the third power of the swath width, for the normal component, and with N_g^{-1} for the parallel. This motivates the use of the split swath for a very accurate estimate of the normal baseline.

Eventually, we relate the interferogram phase variance σ_T^2 in (18) to the final accuracy of the DEM, by assuming that the first term is dominant in (9) and plugging it in (16)

$$\sigma_T^2=\Bigg(k^2\left(\frac{2\pi}{q_{2\pi}}\right)^2\sigma_z^2+k^2\left(\frac{2\pi}{q_{2\pi}}\right)^2$$
$$\sigma_{z\mathrm{GCP}}^2+\left(\frac{B_n\cos\theta}{r_p}\right)^2\sigma_{y\mathrm{GCP}}^2\Bigg)$$
$$\vdots=\left(\frac{B_n}{r\sin\theta}\right)^2\underbrace{\left(\sigma_z^2+\sigma_{z\mathrm{GCP}}^2+\left(\frac{\sin 2\theta}{2}\right)^2\sigma_{y\mathrm{GCP}}^2\right)}_{\sigma_{ZT}^2} \quad (19)$$

with σ_Z^2 being the total noise power, and we finally combine with (18)

$$\sigma_{Bn}\approx\frac{\sqrt{12}}{\sqrt{N_g^3}}\frac{r}{d\cos\theta}\frac{B}{r\sin\theta}\sigma_{ZT}$$
$$\Rightarrow\frac{\sigma_{Bn}}{B_n}=\frac{\sqrt{12}}{\sqrt{N_g^3}}\frac{1}{d\sin\theta\cos\theta}\sigma_{ZT}. \quad (20)$$

As an example, let us assume the typical SRTM spacing $d=90$ m and vertical accuracy of 5 m and say a horizontal accuracy of 20 m [17] to calibrate the normal baseline of a

Ka-band interferometric SAR [5]–[7] with 25° incidence angle, aiming to an HRTI-3 quality DEM with $\sigma_Z = 0.85$ m [22]. Let us assume altitude variations of, for example, 2000 m with respect to the value predicted by GCP (DEMs may have voids in correspondence to steep slopes [1]). If we assume 8-km swath [6] and a vertical accuracy on the output DEM due to a normal baseline of, for example, 0.2 m (which corresponds to a worsening of ∼3% of the vertical accuracy achievable in case of perfect knowledge of geometry), the required relative dispersion of the baseline at far range that results from (10) should be better than $\approx 3\mathrm{e}^{-5}$. An 8-km swath corresponds to $Ng \approx 85$ GCP, and addressing (20) with vertical and horizontal accuracies of GCP of 5 and 20 m, respectively, we get that the achievable relative dispersion is more than ten times higher than the requirement.

Therefore, more than five hundreds of sets of GCPs, which are more than 50-km strip, are necessary. To conclude, more than 5 s of acquisition would be required to calibrate the baseline with single swath, and we would exceed the mechanical stability of the boom. Then, the single-swath approach is not a valid technique for calibration.

V. Accurate Baseline Estimation: The Split-Swath Geometry

The impact of the limitation so far identified increases with the height spread (rough topography), the desired DEM accuracy, the narrowing of the swath (then the improving of resolution [9]), and the displacement between GPC and target to be monitored, which occurs at the swath edges.

The split-swath technique here proposed overcomes the problem by dividing the swath into two strips of half width with a significant gap in between, as shown in Fig. 1, and then mosaicking the strips into the final global DEM. The simultaneous acquisition of the two strips can be achieved in many different ways: with ScanSAR or TOPSAR mode by exploiting electrically steerable antenna or feeder arrays or by interleaving continuous stripmap acquisitions with short bursts from different angles. In this paper, we will refer to the two half swaths as in Figs. 1 and 3. The analysis of such configuration demands for a general formulation where the variation of normal and parallel baselines in the swath cannot be ignored.

We express the interferometric phase as the scalar product between baseline and range versor (1) for each GCP, which can now be placed everywhere in the imaged subswaths. We generalize (2) into the following equation system:

$$\begin{bmatrix} \frac{y_{p,1}+r\sin\theta(P_1)}{r_{p,1}} & \frac{(z_{p1}-r\cos\theta(P_1))}{r_{p,1}} \\ \cdots & \cdots \\ \frac{y_{p,n}+r\sin\theta(P_n)}{r_{p,n}} & \frac{(z_{pn}-\cos\theta(P_n))}{r_{p,n}} \\ \cdots & \cdots \\ \frac{y_{p,Ng}+r\sin\theta(P_{N_g})}{r_{p,Ng}} & \frac{(z_{pNg}-\cos\theta(P_{N_g}))}{r_{p,Ng}} \end{bmatrix} \cdot \begin{bmatrix} B_y \\ B_z \end{bmatrix} = \underline{\Delta R}$$

$$\underline{\underline{\Theta}}_1 \cdot \underline{B} = \underline{d}_1. \quad (21)$$

The assumption is that baseline does not change with the swaths. Indeed, the antenna phase center shifts when switching feeders or by electronically steering the antennas. Here, we assume that such shifts are almost constant within the time scale of boom vibrations, for example, a few seconds [8]. Then, we assume that those shifts are retrieved by a regression led over very long strips.

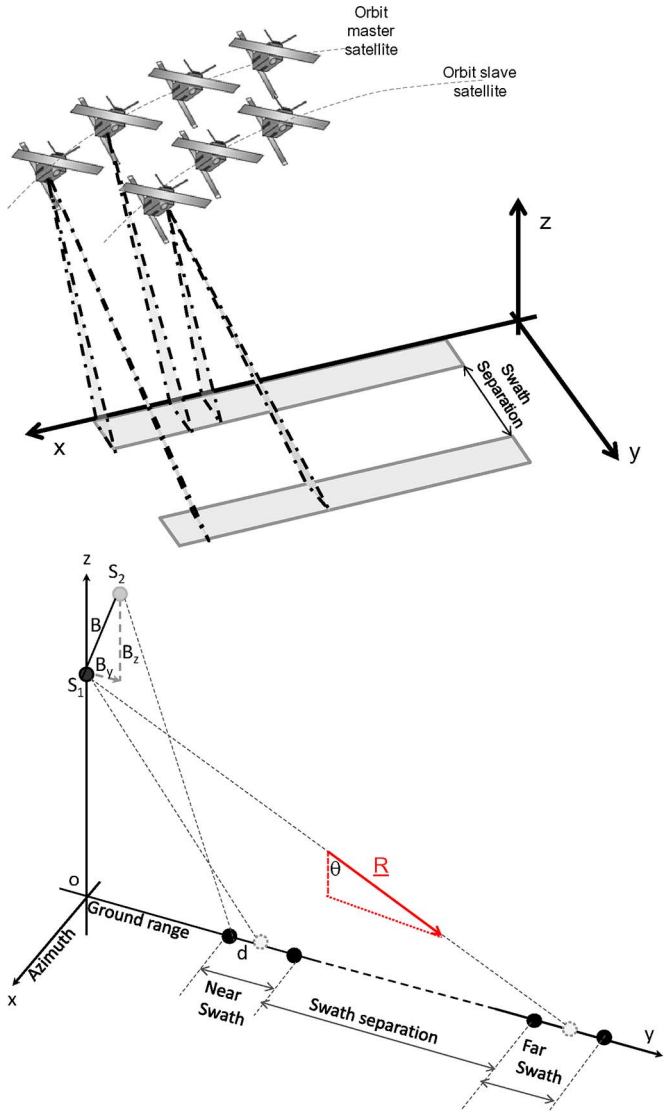

Fig. 3. Graphical representation of the split-swath approach.

A. Inclusion of Image Shifts

The inversion of the baselines should take advantage of the whole information available. In addition to the phases from the GCP, also the local shifts computed during master/slave coregistration [23] should also be exploited. Let us rephrase the differential delay in (3) as follows:

$$\frac{\Delta R_P - \frac{B_n}{r_p}\frac{z_p+y'_P\cos\theta}{\sin\theta}}{1+\frac{y'_p}{r_p}\sin\theta} = -B_p = -B_y\sin\theta + B_z\cos\theta. \quad (22)$$

The values of the range shifts ΔR_P are usually retrieved on a local base (small patches) by coherence maximization during image coregistration [24]. In principle, the knowledge of topography, for example, z_p, is required in (22), but hopefully, its impact is minimized by the scale factor B_n/r_p. We can approximate z_p by the height of the closest GCP; nonetheless,

(22) cannot be used for regressing the normal baseline. We evaluate (22) in a patch centered on each GCP

$$[-\sin\theta(P_{\mathrm{GCP}})+\cos\theta(P_{\mathrm{GCP}})]\cdot\begin{bmatrix}B_y\\B_z\end{bmatrix}\approx\Delta R_{P\mathrm{GCP}}$$
$$-\frac{B_n(P_{\mathrm{GCP}})}{r_{p\mathrm{GCP}}}\frac{z_{p\mathrm{GCP}}}{\sin\theta(P_{\mathrm{GCP}})}=d_2(P_{\mathrm{GCP}}) \quad (23)$$

and then merge the N_g measured shifts $\Delta R_{P\mathrm{GCP}}$ with the N_g equations in (21), leading to the system of $2N_g$ equations and two unknowns

$$\begin{bmatrix}\underline{\underline{\Theta}}_1\\\underline{\underline{\Theta}}_2\end{bmatrix}\cdot\underline{B}=\begin{bmatrix}\underline{d}_1\\\underline{d}_2\end{bmatrix}\Rightarrow\underline{\underline{\Theta}}\cdot\underline{B}=\underline{d}. \quad (24)$$

In order to perform the inversion, we should evaluate the observables $\underline{d}_2$ in (23) and the local incidence angle in $\underline{\underline{\Theta}}$ by assuming *a priori* knowledge of the geometry. We get this by first solving the interferometric location system as in [16] with nominal baselines and then refining the baseline by inverting (24) and iterating once more to get the final DEM. This procedure has been used for the validation presented in the next section.

In the inversion (24), one has to take into account the different accuracy of the differential displacements, measured in correspondence to the GCP $\underline{d}_1$ and the shifts measured in patch coregistration $\underline{d}_2$. The variance of the former is σ_T^2, as in (16), whereas the variance of the latter is a function of the local coherence γ, the range resolution ρ_r, and the number of looks in the patch N_L [24]

$$\sigma_c^2=\frac{3}{2N_L}\frac{1-\gamma^2}{\pi^2\gamma^2}\rho_r^2. \quad (25)$$

The accuracy of the baselines is given by its covariance matrix, from (24)

$$\underline{\underline{C_B}}=(\underline{\underline{\Theta}}^{\mathrm{T}}\underline{\underline{\Theta}})^{-1}\underline{\underline{C}}_d(\underline{\underline{\Theta}}^{\mathrm{T}}\underline{\underline{\Theta}})^{-1} \quad (26)$$

where $\underline{\underline{C}}_d$ is the covariance matrix of the observations in (24), as from (21) and (25)

$$\underline{\underline{C_d}}=E[\underline{d}\underline{d}^{\mathrm{T}}]=\begin{bmatrix}\sigma_T^2\underline{\underline{\mathrm{I}}}_{N_g} & \underline{\underline{0}}\\ \underline{\underline{0}} & \sigma_c^2\underline{\underline{\mathrm{I}}}_{N_g}\end{bmatrix}. \quad (27)$$

The final accuracies σ_{Bn}^2 and σ_{Bp}^2 are evaluated as from (9), by projecting (26) along and across range

$$\underline{\underline{C}}_{Bn}=\begin{bmatrix}\sigma_{Bn}^2 & E[B_nB_p]\\ E[B_nB_p] & \sigma_{Bp}^2\end{bmatrix}=\underline{\underline{\Theta}}_n\underline{\underline{C}}_B\underline{\underline{\Theta}}_n^{\mathrm{T}}$$
$$\underline{\underline{\Theta}}_n=\begin{bmatrix}\cos\theta & \sin\theta\\ -\sin\theta & \cos\theta\end{bmatrix}. \quad (28)$$

VI. Numerical Simulation

The current section is organized as follows: As the first issue, the definition of a requirement on the knowledge of the parallel and normal baselines is derived, and then, the capability of matching this requirement via single- and split-swath calibrations is investigated. To conclude, the split-swath calibration is used in a numeric simulation to create a super HRTI-3 DEM (i.e., better horizontal resolution, for example, 2×2 m^2, and the same vertical accuracy: $\sigma_Z=0.85$ m). The parameters of the system are summarized in Table I.

TABLE I
Numerical Simulation Parameters

Parameter	Value
Satellite height	450 km
Monostatic system	p = 2
Mid swath incidence angle	25°
Swath width	4 + 4 km
Carrier frequency	35 GHz (Ka-band)
Boom length	25 m
GCP resolution	90 x 90 m^2
GCP vertical accuracy	5 m
GCP horizontal accuracy	20 m
SNR	15 dB
SLC resolution	1 x 1 m^2
Multi looked resolution	2 x 2 m^2
Altitude variation w.r.t. nearest GCP	2000 m

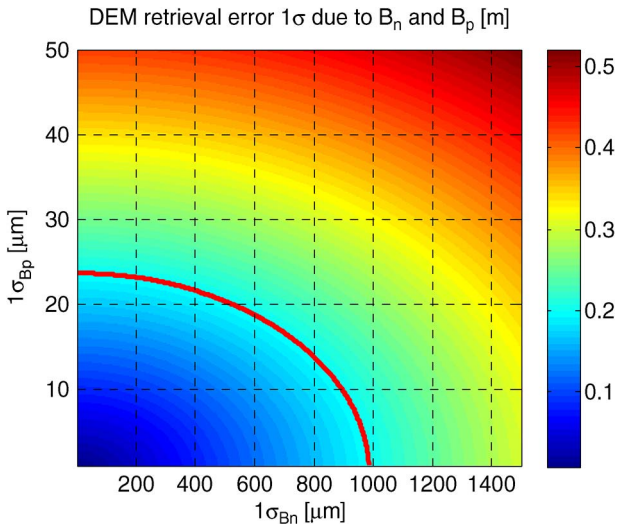

Fig. 4. DEM accuracy σ_z due to the nonperfect knowledge of the normal and parallel baselines. The red line marks the requirement.

The requirements on both normal and parallel baselines are derived evaluating (9) for the parameters in Table I. The DEM accuracy is represented in Fig. 4, in the case where the sole uncertainties are the normal and parallel baselines, the second and third elements in (9). The red line marks the requirement on the baseline accuracy by imposing that they affect the DEM vertical standard deviation with less than 20 cm, i.e., ∼3% of the total budget (85 cm). From Fig. 4, we observe that baseline knowledge should be on the order of tens of micrometers, particularly for the parallel baseline. Such a requirement compares with the 40-μm budget that was achieved on the airborne demonstrator for GLISTIN [18]. Getting such accuracy out of long boom subject to vibrations within a few hertz is indeed a challenge.

Then, we address the potentials provided by the prior SRTM DEM to calibrate for baseline. The achievable baseline accuracies have been evaluated according to the model in Section V, in the single- and split-swath cases, also including the images' shift information. The covariance matrix of baselines is computed starting from (28). The elements on its diagonal are the achievable accuracies for the normal and parallel components: They are plotted in Fig. 5 as a function of the azimuth strip

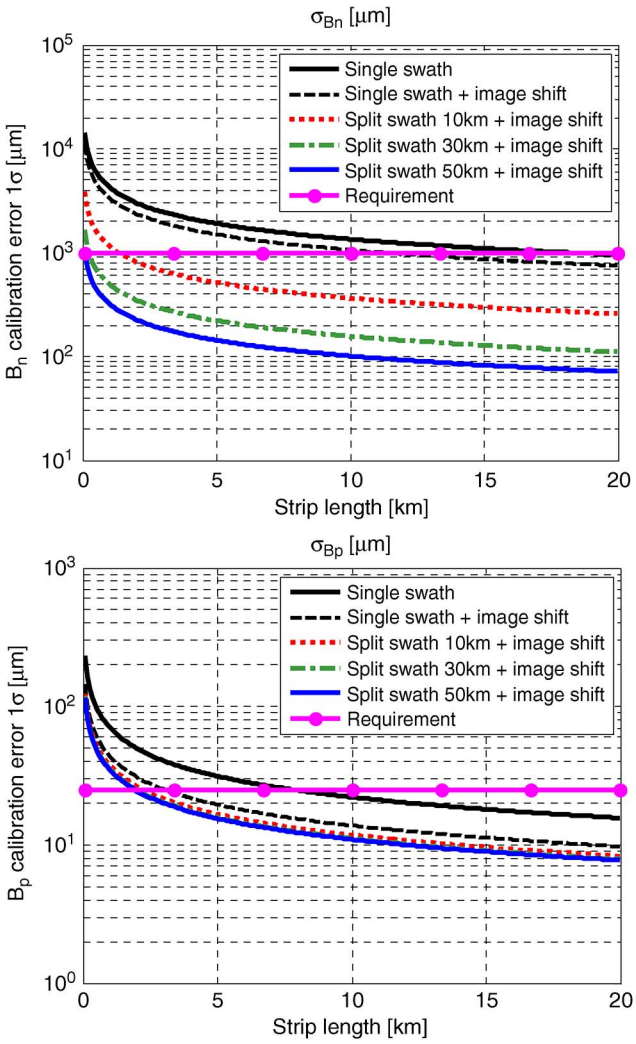

Fig. 5. Accuracy achievable on the (top panel) normal and (bottom panel) parallel baselines as a function of the azimuth strip length compared to the (horizontal line with dots) requirement. The (solid black line) classic single-swath technique is compared to the accuracy achievable considering image shift and the (dashed line) novel split-swath method. With split swath, three distances between swaths have been considered: (Red dotted line) 10 km, (green dashed–dotted line) 30 km, and (blue solid line) 50 km.

length necessary to meet the requirements on normal and parallel baselines as from Fig. 4. We compare the single-swath technique with the novel split-swath method for distances between the two swaths of 10, 30, and 50 km.

The results on normal baseline lighten up the advantages of the novel split-swath method with respect to the single-swath technique.

Fig. 5 top panel clearly shows the power of the split-swath calibration on normal baseline: The performances increase drastically. With a separation of 50 km, the requirement of $\approx$1 mm on the normal baseline is met even with a 2-km strip (corresponding to much less than 0.5 s of acquisition). The calibration is made possible by the split-swath method, and it paves the way for a super HRTI-3 DEM. On the other hand, the single-swath stripmap mode would need to process a 15–20-km-long strip to calibrate the normal baseline up to the required accuracy (as also anticipated at the end of Section IV). Then, the boom should be stable with a time interval of 2–3 s.

The results on parallel baseline point out the advantage of using image shift coefficients (black dashed line) with respect to the so far used single-swath technique based on GCP (black solid line). A parallel baseline is less sensitive than a normal baseline to split swath. Nevertheless, split-swath calibration and, mainly, the inclusion of image shift coefficients allow for more than half the strip length with respect to the classic single-swath calibration. In the case of 50 km of separation, the requirement on the parallel baseline is met with less than 5-km strip (i.e., less than 1 s of acquisition).

These results are crucial as they show that the overall required vertical accuracy (i.e., $\sigma_Z = 0.85$ m) can be reached only by having a very good accuracy on the baseline, implying the need of a calibration step. The novel split-swath calibration overcomes the limitations of single-swath calibration as it is the only technique that can ensure the required accuracy on normal baseline with a reasonably short acquisition (i.e., less than 1 s). Using image shifts enables a strong reduction of the strip length necessary to meet the requirement on the accuracy of parallel baseline.

Finally, the generation of a super HRTI-3 DEM is considered. A numeric simulator for mountainous topography nearby Las Vegas has been set up. The parameters of the system reported in Table I have been used for the simulation. The calibration is considered using as GCP the points from SRTM. Two separated swaths, each with an extension of 4 km in ground range, have been simulated. The strip length ranges from 1.5 to 5 km, while the swath separation varies from 10 to 50 km. Significant harmonic errors of $\sim$3 mm on normal baseline (i.e., B_n) and $\sim$1 mm for parallel baseline (i.e., B_p) at slow frequency (i.e.,: < 0.1 Hz) have been considered.

The results of the experiment, in terms of accuracy on both normal and parallel baselines, are represented in Fig. 6. A 2-D parabolic fitting of the standard deviation has been done to point out the trend of the measurements. It is relevant that the values of accuracy and the trends are comparable with the one presented in Fig. 5.

In particular, notice that the accuracy on the normal baseline strongly depends on both strip length and swath separation, while for parallel baseline, the accuracy is less sensitive to swath separation, as in Fig. 5.

We considered the creation of a high-resolution (i.e., 2 m by 2 m) and high-accuracy ($\sigma_Z = 0.85$ m) DEM for the case of 4 km by 5 km (i.e., range by azimuth) swath size and 50 km of separation between the two swaths. Fig. 7 reports two scatter plots: one for the input GCP from SRTM and one for the output super HRTI-3 DEM. Notice the crucial enhancement of both accuracy and resolution between the two DEMs, the one used for calibration and the one produced by the interferometer. The first has an accuracy σ of 90 $\times$ 90 (horizontal) $\times$ 10 m, while the second of $2 \times 2 \times 0.8$ m. The result is enlightened in Fig. 8, where the vertical error of the output super HRTI-3 DEM is represented versus the overall vertical error of the input SRTM DEM [the error derived from the spatial location error of the GCP addressed in (19)] addressing the same set of GCPs. These results achieved by numerical simulations validate both the performance evaluation in Section V and the bounds established at the beginning of this section.

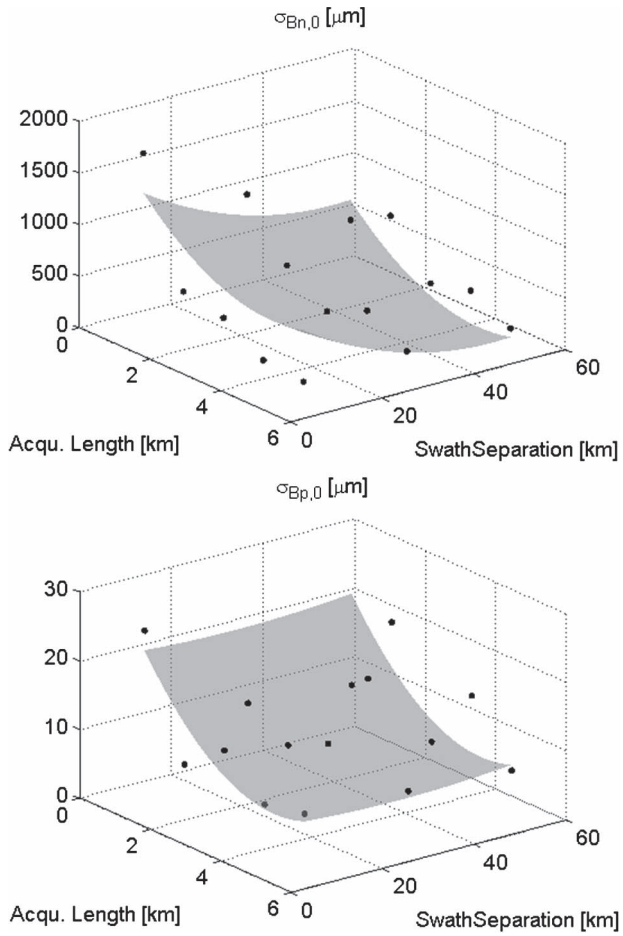

Fig. 6. Accuracies of the (top panel) normal baseline $B_{n,0}$ and (bottom panel) parallel baseline B_{p0}, referred to 25 looks/incidence angles, as a function of swath separation and acquisition length. (Dots) Experimental results are a cloud around the surface that is the 2-D parabolic regression of the points.

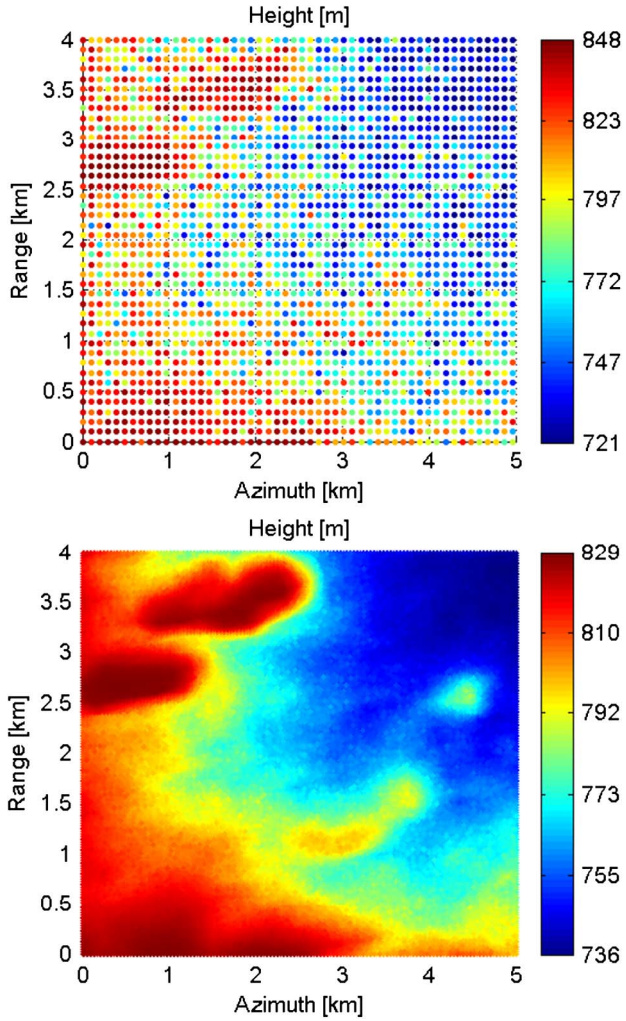

Fig. 7. (Top panel) Low-resolution coarse-accuracy reference DEM. (Bottom panel) New high-resolution high-accuracy DEM achievable after baseline calibration.

VII. Conclusion

This paper has proposed a method to generate a high-resolution DEM by exploiting a preexisting DEM at coarse resolution as a set of GCPs, to provide the calibration of the system parameters (i.e., mainly baselines). We have proposed a mathematical model to jointly take into account information coming from input coarse DEM and local shifts computed during image coregistration. The model allows one to evaluate both horizontal and vertical accuracies of the output high-quality DEM. Moreover, referring to vertical accuracy, the impact rising from baselines' knowledge has been characterized. The requirement on the baselines' accuracy turned out to be very stringent (i.e., up to tens of micrometers), and we have proven that it can be hardly met applying the so far used calibration techniques to the new generation of SAR system, which are characterized by high resolution and narrow swath. This could limit the capability of calibrating baselines up to the required values, thus preventing the generation of high-resolution and high-accuracy DEM from single-pass interferometry. To overcome the limitation, we have proposed as possible solution a novel calibration technique, named "split swath." The approach fruitfully exploits multi-swath SAR acquisition modes (i.e., ScanSAR or TOPSAR) to acquire two strips with significant diversity in incidence angle. We have presented a theoretical approach, mainly based on linearization, to estimate baselines and to evaluate the accuracy achievable on both baselines and DEM. We applied the model to analyze a possible future single-pass SAR interferometer working in Ka-band. The results proved that, with two sensors placed at the two tips of a 25-m-long boom, it is possible to generate a better-than-HRTI3 DEM. We validated the theoretical results by setting up an independent simulator that is able to take into account both the baselines' calibration and DEM generation. The experimental results, presented in the dedicated section, revealed to be in accordance to the theoretical predicted performances, thus providing confirmation of the reliability of both the proposed split-swath technique and the performance model.

Appendix

Model for Localization Accuracy

The model of the observables from an interferometric SAR can be expressed by the azimuth (zero Doppler), range, and differential delays, like the approximation for constant incidence angle in (3).

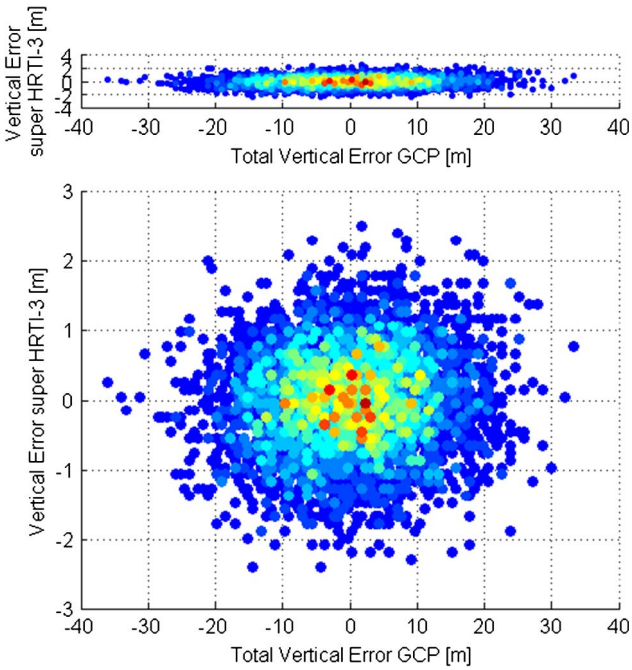

Fig. 8. Scatter plot of the vertical error of the output super HRTI-3 DEM versus the total vertical error of the input SRTM DEM for the same set of GCPs. The colormap refers to the probability density function of the errors. In the top panel, we use proportional axes to enlighten different error dispersion. The bottom panel reports the details around zero for vertical error on the output super-HRTI-3 DEM (i.e., y-axis).

It is a set of three nonlinear equations, where the dependence upon the target position $\underline{P}$ and the baselines (and maybe other orbit parameters) $\underline{B}$ has been made explicit. As we assume a small error, we compute the total differential of (3) in respect of the two sets of unknowns in the optimum, as in (6), and invert it to find the error on the target location that we are interested in

$$\underline{\Delta}_d = \underline{\underline{J}}_P \underline{\Delta}_P + \underline{\underline{J}}_B \underline{\Delta}_B \Rightarrow \underline{\Delta}_P = \underline{\underline{J}}_P^{-1}(\underline{\Delta}_d - \underline{\underline{J}}_B \underline{\Delta}_B). \quad (1a)$$

The accuracy achievable is given by the covariance matrix

$$\begin{aligned}\underline{\underline{C}}_{\Delta_P} &= E\left[\underline{\Delta}_P \underline{\Delta}_P^{\mathrm{T}}\right] \\ &= \underline{\underline{J}}_p^{-1} \underline{\underline{C}}_{\Delta_d} \left(\underline{\underline{J}}_p^{-1}\right)^{\mathrm{T}} + \underline{\underline{J}}_p^{-1} \underline{\underline{J}}_B \underline{\underline{C}}_{\Delta_B} (\underline{\underline{J}}_B)^{\mathrm{T}} \left(\underline{\underline{J}}_p^{-1}\right)^{\mathrm{T}}. \quad (2a)\end{aligned}$$

If the baselines are known without error (see Section III-A1), the rightmost term is zero. The covariance derived by exploiting (3) is

$$\begin{aligned}\underline{\underline{C}}_{\Delta_P} &= \underline{\underline{J}}_p^{-1} \underline{\underline{C}}_{\Delta_d} \left(\underline{\underline{J}}_p^{-1}\right)^{\mathrm{T}} \\ &= \begin{bmatrix} 1 & 0 & 0 \\ 0 & 1/\sin\theta & 0 \\ 0 & B_y/B_n & \frac{r\cdot\sin\theta}{B_n} \end{bmatrix} \cdot \begin{bmatrix} \sigma_x^2 & 0 & 0 \\ 0 & \sigma_r^2 & 0 \\ 0 & 0 & (\lambda/2p\pi)^2\sigma_\phi^2 \end{bmatrix} \\ &\quad \cdot \begin{bmatrix} 1 & 0 & 0 \\ 0 & 1/\sin\theta & B_y/B_n \\ 0 & 0 & r\cdot\sin\theta/B_n \end{bmatrix}. \quad (3a)\end{aligned}$$

The terms on the diagonal express the accuracy of each component

$$\begin{aligned}\sigma_x^2 &= \sigma_x^2 \\ \sigma_y^2 &= \frac{\sigma_r^2}{\sin^2\theta} \\ \sigma_z^2 &= \left(\frac{B_y}{B_n}\right)^2 \sigma_r^2 + \left(\frac{\sin\theta}{B_n} r \left(\frac{\lambda}{2p\pi}\right)\sigma_\phi\right)^2. \quad (4a)\end{aligned}$$

This last expression compares with (8).

If baselines and other parameters are to be estimated, for example, from GCP, a second system of equations similar to (3) has to be solved for the unknown parameters. Here, again, we compute the total differential to relate the accuracy of the baseline estimation with that of the GCP and the noise on SAR interferogram (range, azimuth, and phase)

$$\underline{\Delta}_{dg} = \underline{\underline{J}}_{Pg} \underline{\Delta}_{Pg} + \underline{\underline{J}}_{Bg} \underline{\Delta}_{Bg} \quad (5a)$$

where the suffix "g" reminds that (5a) applies to GCP. If the number of GCPs is much larger than the parameters to be estimated, as it is desired, the following equation is to be pseudoinverted to estimate the baseline accuracy:

$$\underline{\Delta}_{Bg} = \underline{\underline{J}}_{Bg}^{\perp}(\underline{\Delta}_{dg} + \underline{\underline{J}}_{Pg} \underline{\Delta}_{Pg}) \quad (6a)$$

where the apex "$\perp$" stands for the Moore–Penrose pseudoinverse $\underline{\underline{J}}_{Bg}^{\perp} = (\underline{\underline{J}}_{Bg}^{\mathrm{T}} \underline{\underline{J}}_{Bg})^{-1} \underline{\underline{J}}_{Bg}^{\mathrm{T}}$. We can merge other information, like image shifts, by implementing a weighted pseudoinversion as in Section V. The accuracy of baseline estimation is given by the covariance of (6a)

$$\begin{aligned}\underline{\underline{C}}_{\Delta_B} &= E\left[\underline{\Delta}_{Bg} \underline{\Delta}_{Bg}^{\mathrm{T}}\right] \\ &= \underline{\underline{J}}_{Bg}^{\perp} \underline{\underline{C}}_{\Delta dg} \underline{\underline{J}}_{Bg}^{\perp} + \underline{\underline{J}}_{Bg}^{\perp} \underline{\underline{J}}_{Pg} \underline{\underline{C}}_{\Delta_{Pg}} \underline{\underline{J}}_{Pg}^{\mathrm{T}} \underline{\underline{J}}_{Bg}^{\perp}. \quad (7a)\end{aligned}$$

The error in baselines has been related both to the error on the interferogram phase, range, azimuth and to the noise in the GCP. The final DEM accuracy is given by the covariance of target location, i.e., by combining (2) and (7)

$$\begin{aligned}\underline{\underline{C}}_{\Delta_P} &= \underline{\underline{J}}_p^{-1} \underline{\underline{C}}_{\Delta_d} \left(\underline{\underline{J}}_p^{-1}\right)^{\mathrm{T}} + \underline{\underline{J}}_p^{-1} \underline{\underline{J}}_B \underline{\underline{J}}_{Bg}^{\perp} \underline{\underline{C}}_{\Delta_{dg}} \underline{\underline{J}}_{Bg}^{\perp} \underline{\underline{J}}_B^{\mathrm{T}} \left(\underline{\underline{J}}_p^{-1}\right)^{\mathrm{T}} \\ &\quad + \underline{\underline{J}}_P^{-1} \underline{\underline{J}}_B \underline{\underline{J}}_{Bg}^{\perp} \underline{\underline{J}}_{Pg} \underline{\underline{C}}_{\Delta_{Pg}} \underline{\underline{J}}_{Pg}^{\perp} \underline{\underline{J}}_{Bg}^{\mathrm{T}} \underline{\underline{J}}_B^{\mathrm{T}} \left(\underline{\underline{J}}_p^{-1}\right)^{\mathrm{T}}. \quad (8a)\end{aligned}$$

The three components are as follows:

1) the contribution of the uncertainties on SAR measures (range, Doppler, and phase) on the target to be located; this is the unavoidable effect of thermal noise;
2) a similar contribution affecting the target in correspondence to the GCP;
3) the inaccuracy of GCP, for example, the prior DEM.

Notice that the pseudoinversion of the Jacobean $\underline{\underline{J}}_{Bg}^{\perp}$ relative to the estimate of the baseline from GCP tends to zero as the number of GCPs increases. This is somewhat the desired solution, i.e., we must design the calibration system in order to leave only the effect of thermal noise on the observed data.

ACKNOWLEDGMENT

The authors would like to thank Prof. F. Rocca for the hint about the split-swath configuration as a possible fruitful technique to enhance the accuracy in the baseline calibration.

REFERENCES

[1] T. G. Farr, P. A. Rosen, E. Caro, R. Crippen, R. Duren, S. Hensley, M. Kobrick, M. Paller, E. Rodriguez, L. Roth, D. Seal, S. Shaffer, J. Shimada, J. Umland, M. Werner, M. Oskin, D. Burbank, and D. E. Alsdorf, "The Shuttle Radar Topography Mission," *Rev. Geophys.*, vol. 45, no. 2, pp. RG2004-1–RG2004-33, Jun. 2007.

[2] B. Rabus, M. Eineder, A. Roth, and R. Bamler, "The Shuttle Radar Topography Mission—A new class of digital elevation models acquired by spaceborne radar," *ISPRS J. Photogramm. Remote Sens.*, vol. 57, no. 4, pp. 241–262, Feb. 2003.

[3] A. Moreira, "TanDEM-X: A high resolution radar topography mission," in *Proc. IRS*, Sep. 7–9, 2011, pp. 30–31.

[4] M. Shirzaei and T. R. Walter, "Estimating the effects of satellite orbital error using wavelet based robust regression applied to InSAR deformation data," *IEEE Trans. Geosci. Remote Sens.*, vol. 49, no. 11, pp. 4600–4605, Nov. 2011.

[5] C. Germani, R. Venturini, M. Ludwig, E. Daganzo-Eusebio, S. D"Addio, and A. Gabriele, "Ka-band SAR interferometer," in *Proc. IEEE IGARSS*, Jul. 22–27, 2012, pp. 5598, 5601.

[6] M. Ludwig, S. D"Addio, M. Aguirre, J. C. Angevain, E. Saenz, and K. Engel, "Imaging Ka-band SAR interferometer," in *Proc. 3rd Int. APSAR Conf.*, Sep. 26–30, 2011, pp. 1, 4.

[7] C. Schaefer and P. Lopez-Dekker, "Interferometric Ka-band SAR with DBF capability," in *Proc. 9th EUSAR Conf.*, Apr. 23–26, 2012, pp. 7, 10.

[8] J. W. Umland and H. Eisen, "SRTM on orbit structural dynamics," presented at the 42nd Structures, Structural Dynamics, Materials Conf. American Institute of Aeronautics and Astronautics, Seattle, WA, USA, 2001, Paper AIAA 2001-1588.

[9] A. Freeman, W. Johnson, B. Huneycutt, R. Jordan, S. Hensley, P. Siqueira, and J. Curlander, "The "myth" of the minimum SAR antenna area constraint," in *Proc. IEEE IGARSS*, 1999, vol. 3, pp. 1770, 1772.

[10] R. K. Moore, J. P. Claassen, and Y. H. Lin, "Scanning spaceborne synthetic aperture radar with integrated radiometer," *IEEE Trans. Aerosp. Electron. Syst.*, vol. AES-17, no. 3, pp. 410–421, May 1981.

[11] A. Currie, "Wide-swath SAR imaging with multiple azimuth beams," in *Proc. IEE Colloq. Synthetic Aperture Radar*, Nov. 29, 1989, pp. 3/1, 3/4.

[12] F. De Zan and A. Monti Guarnieri, "TOPSAR: Terrain observation by progressive scans," *IEEE Trans. Geosci. Remote Sens.*, vol. 44, no. 9, pp. 2352–2360, Sep. 2006.

[13] C. Buck, M. Aguirre, C. Donion, D. Petrolati, and S. D'Addio, "Steps towards the preparation of a wavemill mission," in *Proc. IEEE IGARSS*, Jul. 24–29, 2011, pp. 3959–3962.

[14] R. Bamler and P. Hartl, "Synthetic aperture radar interferometry," *Inverse Prob.*, vol. 14, no. 4, pp. R1–R54, Aug. 1998.

[15] P. A. Rosen, S. Hensley, I. R. Joughin, K. L. Fuk, S. N. Madsen, E. Rodriguez, and R. M. Goldstein, "Synthetic aperture radar interferometry," *Proc. IEEE*, vol. 88, no. 3, pp. 333, 382, Mar. 2000.

[16] E. Sansosti, "A simple and exact solution for the interferometric and stereo SAR geolocation problem," *IEEE Trans. Geosci. Remote Sens.*, vol. 42, no. 8, pp. 1625–1634, Aug. 2004.

[17] A. Koch and C. Heipke, "Quality assessment of digital surface models derived from the Shuttle Radar Topography Mission (SRTM)," in *Proc. IEEE IGARSS*, 2001, pp. 2863–2865.

[18] D. Moller, S. Hensley, G. A. Sadowy, C. D. Fisher, T. Michel, M. Zawadzki, and E. Rignot, "The glacier and land ice surface topography interferometer: An airborne proof-of-concept demonstration of high-precision Ka-band single-pass elevation mapping," *IEEE Trans. Geosci. Remote Sens.*, vol. 49, no. 2, pp. 827–842, Feb. 2011.

[19] V. M. Enjolras and E. Rodriguez, "An assessment of a Ka-band radar interferometer mission accuracy over Eurasian rivers," *IEEE Trans. Geosci. Remote Sens.*, vol. 47, no. 6, pp. 1752–1765, Jun. 2009.

[20] R. F. Hanssen, *Radar Interferometry: Data Interpretation and Error Analysis*, 2nd ed. Berlin, Germany: Springer-Verlag, 2005.

[21] L. Iannini and A. Monti Guarnieri, "Atmospheric phase screen in ground based radar: Statistics and compensation," *IEEE Geosci. Remote Sens. Lett.*, vol. 8, no. 3, pp. 537–541, May 2011.

[22] J. H. Gonzalez, M. Bachmann, G. Krieger, and H. Fiedler, "Development of the TanDEM-X calibration concept: Analysis of systematic errors," *IEEE Trans. Geosci. Remote Sens.*, vol. 48, no. 2, pp. 716–726, Feb. 2010.

[23] D. O. Nitti, K. F. Hanssen, R. F. Refice, A. Bovenga, and F. Nutricato, "Impact of DEM-assisted coregistration on high-resolution SAR interferometry," *IEEE Trans. Geosci. Remote Sens.*, vol. 49, no. 3, pp. 1127–1143, Mar. 2011.

[24] R. Bamler, "Interferometric stereo radargrammetry: Absolute height determination from ERS-ENVISAT interferograms," in *Proc. IEEE IGARSS*, 2000, pp. 742–745.